Journal of Solid State Chemistry 181 (2008) 2285–2291

Contents lists available at ScienceDirect

Journal of Solid State Chemistry

journal homepage: www.elsevier.com/locate/jssc

Aluminium substitution in iron(II–III)-layered double hydroxides: Formation and cationic order

Christian Ruby [a,*], Mustapha Abdelmoula [a], Rabha Aissa [a], Ghouti Medjahdi [b], Michela Brunelli [c], Michel François [b]

[a] Laboratoire de Chimie Physique et Microbiologie pour l'Environnement, LCPME UMR7564 CNRS-Nancy Université, 405 rue de Vandoeuvre, 54600 Villers-lès-Nancy, France
[b] Laboratoire de Chimie du Solide Minéral, LCSM UMR 7555 CNRS-Nancy Université, Faculté des Sciences, BP239, 54506 Vandoeuvre-lès-Nancy, France
[c] European Synchrotron Radiation Facility (ESRF), 6 rue Jules Horowitz, BP 220, 38043 Grenoble Cedex, France

ARTICLE INFO

Article history:
Received 28 January 2008
Received in revised form
5 May 2008
Accepted 12 May 2008
Available online 24 May 2008

Keywords:
Green rust
Rietveld
X-ray diffraction
Mössbauer

ABSTRACT

The formation and the modifications of the structural properties of an aluminium-substituted iron(II–III)-layered double hydroxide (LDH) of formula $Fe^{II}_4Fe^{III}_{(2-6y)}Al^{III}_{6y}(OH)_{12}SO_4, 8H_2O$ are followed by pH titration curves, Mössbauer spectroscopy and high-resolution X-ray powder diffraction using synchrotron radiation. Rietveld refinements allow to build a structural model for hydroxysulphate green rust, GR(SO_4^{2-}), i.e. $y = 0$, in which a bilayer of sulphate anions points to the Fe^{3+} species. A cationic order is proposed to occur in both GR(SO_4^{2-}) and aluminium-substituted hydroxysulphate green rust when $y < 0.08$. Variation of the cell parameters and a sharp decrease in average crystal size and anisotropy are detected for an aluminium content as low as $y = 0.01$. The formation of Al-GR(SO_4^{2-}) is preceded by the successive precipitation of Fe^{III} and Al^{III} (oxy)hydroxides. Adsorption of more soluble Al^{III} species onto the initially formed ferric oxyhydroxide may be responsible for this slowdown of crystal growth. Therefore, the insertion of low aluminium amount ($y \sim 0.01$) could be an interesting way for increasing the surface reactivity of iron(II–III) LDH that maintains constant the quantity of the reactive Fe^{II} species of the material.

1. Introduction

Layered double hydroxides (LDHs) are represented by the general formula $[M^{II}_{(1-x)}M^{III}_x(OH)_2]^{x+}$ $[(x/n)\ A^{n-},\ mH_2O]^{x-}$ where both M^{II} and M^{III} are metallic cations located in positively charged brucite-type sheets separated by interlayers made of anions A^{n-} and water molecules [1–4]. Iron(II–III) LDHs, commonly called green rust (GR), are interesting compounds due to the presence of the reactive Fe^{II} cations that can easily reduce anionic pollutants such as nitrate [5], selenate [6] or chromate [7] . The overall spectra of LDHs have received increasing interest in recent years owing to their applications as catalysts, adsorbents and ion exchangers [8]. Formation of LDHs is governed by many parameters such as the nature of the cations, the pH of precipitation, temperature and the precipitation method. Physical parameters that can be controlled are the crystal size, morphology and specific surface area (SSA) for optimizing the LDH reactivity. For instance, hydrothermal treatment or biogenic synthesis is known to increase the crystal size of LDHs [9,10]. Prinetto et al. [11] demonstrated that LDHs prepared by a sol–gel synthesis route had a higher SSA than those obtained by the classical co-precipitation method. Another way to modify the microstructural properties of the LDHs is to substitute the M^{II} or M^{III} cations by another kind of cations. For instance, Carja et al. [12] were able to increase the SSA of hydrotalcite $Mg_6Al_2(OH)_{16}CO_3 \cdot 4H_2O$ by a partial substitution of the Mg^{II} cations by Fe^{II} species. Substitution of the divalent Fe^{II} cation by Mg^{II} was also previously performed for GR-type LDHs [13].

The ordering/disordering properties of the LDHs were the subject of a number of studies [1–3,14–18]. Radha et al. [15] studied the M^{II}–Al^{III}–CO_3^{2-} LDHs (M = Ni or Co) structural order as a function of the nature of the intercalated anion. Solids with a greater degree of order were observed for CO_3^{2-}, Cl^- and SO_4^{2-} anions whereas stacking turbostratic disorder was evidenced for anions that did not match the symmetry of the interlayers sites, e.g. ClO_4^-, BrO_3^- and NO_3^-. Structural refinements were also performed for hydrotalcite by Bellotto et al. [16] and more recently for the hydroxycarbonate GR {GR(CO_3^{2-})} [18]. The spatial group of carbonated LDHs is generally $R\bar{3}m$ with $a \approx 3.17$ Å and $c \approx 22.70$ Å and long-range order of the iron cations was not observed [14,16,18]. On the contrary, a long-range superstructure ordering was observed with conventional X-ray diffraction (XRD) for the sulphated form of GR {GR(SO_4^{2-})} that crystallized in a trigonal structure $P\bar{3}1m$ with $a = 5.524$ Å and $c = 11.01$ Å [17].

* Corresponding author.
E-mail address: Christian.ruby@lcpme.cnrs-nancy.fr (C. Ruby).

0022-4596/$ - see front matter © 2008 Elsevier Inc. All rights reserved.
doi:10.1016/j.jssc.2008.05.027

The $a\sqrt{3}$superstructure leads to the existence of the two crystallographic sites 2*c* and 1*a* possibly occupied by the cations Fe^{3+} and Fe^{2+}, respectively. The larger interlayer spacing, i.e. ~11 Å instead of ~7.6 Å for GR(CO_3^{2-}), was attributed to the presence of a bilayer of SO_4^{2-} anions and water molecules. Nevertheless, the exact orientation of the sulphate anions was not fully established. Four models taking into account the two possible orientations of the sulphate group (up and down) and two positions in (*a*, *b*) plane, one below Fe^{3+} and the other below Fe^{2+} was proposed to interpret conventional XRD patterns. The two models "down to Fe^{3+}" and "up to Fe^{3+}" led to equivalent and satisfactory agreement factors; thus ambiguities remain concerning the orientation of the sulphate groups. Higher-resolution X-ray data should clarify this point.

It was also shown that the substitution of aluminium in GR(SO_4^{2-}) can occur [19]. The proposed chemical formula of the substituted compound was $Fe^{II}_4\ Fe^{III}_{(2-6y)}\ Al^{III}_{6y}\ (OH)_{12}\ SO_4,\ 8H_2O$ {Al–GR(SO_4^{2-})} where *y* represents the aluminium molar fraction of the compound, i.e. $y = n(Al^{III})/[n(Fe^{II})+n(Fe^{III})+n(Al^{III})]$. As previously discussed [19,20], the use in the initial mixture of the relative molar concentration expected from this chemical formula led to the formation of ~ 95% of Al-GR(SO_4^{2-}) and ~5% of another magnetic compound as shown by Mössbauer spectroscopy. The composition of the initial solution corresponds to the square points situated on the tie-line L_1 in the ternary mass-balance diagram presented in Fig. 1. L_1 joins sulphated green rust $Fe^{II}_4\ Fe^{III}_2\ SO_4,\ 8H_2O$ (point B) to the hypothetical "fully" substituted $Fe^{II}_4\ Al^{III}_2\ (OH)_{12}\ SO_4,\ 8H_2O$ compound (point C). However, the existence of caresite that obeys a similar chemical formula $Fe^{II}_4Al^{III}_2(OH)_{12}CO_3,\ 3H_2O$ was reported [21].

In this paper, the pH titration curves obtained during the co-precipitation of {Fe^{II}, Fe^{III}, Al^{III}} mixtures are studied. The different steps of precipitation that precede the formation of Al-GR(SO_4^{2-}) are determined. The quantity of Fe^{III} sites occupied by the Al^{III} cations present in the solution is indirectly calculated by using the adjustments of Mössbauer spectra. Then, the structural properties of Al-GR(SO_4^{2-}) are evaluated by Rietveld refinements for increasing the quantity of aluminium. Previous studies using conventional powder XRD [19,20] showed a strong loss of intensity and a broadening of the diffraction lines especially when the aluminium molar fraction *y* of the Al-GR(SO_4^{2-}) compounds was higher than 0.1. For this reason, samples containing lower aluminium content were prepared in this work ($0 \leqslant y \leqslant 0.08$) and high-resolution X-ray powder diffraction (HRXRPD) patterns were recorded at the European Synchroton Radiation Facility (ESRF, Grenoble France). The evolution of the structural and microstructural properties of GR(SO_4^{2-}) as a function of Al^{3+} substitution is discussed. The four structural models differing only by the sulphate group orientation are revisited on the basis of this new HRXRPD data.

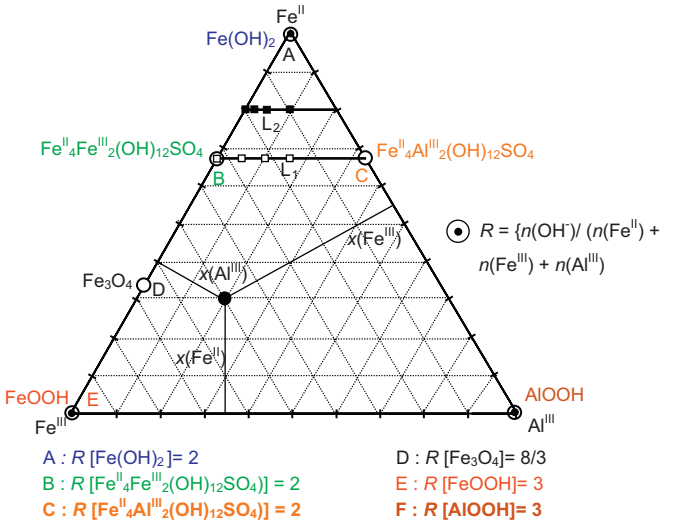

Fig. 1. Mass-balance diagram showing different compounds of the ternary {Fe^{II}, Fe^{III}, Al^{III}} system. The third dimension corresponds to the ratio *R*, that is the number of OH^- species consumed per mole of total cations for the precipitation of a given compound. Lines L_1 and L_2 correspond to a value $R = 2$.

2. Experimental

2.1. Sample synthesis

The samples were prepared by a co-precipitation method performed in 1 L glass reactor under a continuous flux of nitrogen to avoid any oxidation of the Fe^{II} species. With the help of a peristaltic pump, 150 mL of an NaOH solution (0.8 M) was progressively added into a 600 mL solution containing the Fe^{II}, Fe^{III} and Al^{III} species obtained by dissolving $FeSO_4,\ 7H_2O$, $Fe^{III}_2(SO_4)_3,\ 5H_2O$ and $Al^{III}(SO_4)_3,\ 5H_2O$ salts, respectively. The duration of a typical titration experiment is ~4 h. The total concentration $C = [Fe^{II}]_0+[Fe^{III}]_0+[Al^{III}]_0$, where $[Fe^{II}]_0$, $[Fe^{III}]_0$ and $[Al^{III}]_0$ are the concentration of each soluble cations of the initial solution, was maintained constant at 6.67×10^{-2} M. As mentioned previously [20], 100% of aluminium-substituted GR was obtained by preparing the sample in an excess of ferrous and hydroxyl species, i.e. molar ratios $x(Fe^{II})_0 = n(Fe^{II})_0/\{n(Fe^{II})_0+n(Fe^{III})_0+n(Al^{III})_0\} = 0.2$ and $n(OH^-)/[n(Fe^{III})_0+n(Al^{III})_0] = 7$ (instead of 6) were employed. Possible explanations concerning the use of these particular conditions for the preparation of GR(SO_4^{2-}) were given in previous studies [20,22]. The molar fraction of aluminium in the initial solution $x(Al^{III})_0 = n(Al^{III})_0/\{n(Fe^{II})_0+n(Fe^{III})_0+n(Al^{III})_0\}$ was varied between 0 and 0.1. It corresponds to an expected molar fraction of aluminium *y* in the solid Al-GR(SO_4^{2-}) compound that varies between 0 and 0.17. The composition of the initial solution used in this study corresponds to the square points situated on the tie-line L_2 in Fig. 1. The excess of Fe^{II} species used for the synthesis corresponds to the distance of separation between lines L_1 and L_2.

2.2. Samples characterization

The suspensions were filtered in a glove box filled with a nitrogen inert atmosphere, set in the sample holder and introduced in the cryostat set at a temperature of 78 K for transmission Mössbauer spectroscopy (TMS) measurements. TMS spectra were measured by means of a constant-acceleration spectrometer with a 50 mCi source of ^{57}Co in Rh. Isomer shift is reported with respect to metallic α-iron at room temperature used as a reference. Adjustments of the spectra were performed using Lorentzian-shape lines.

For the HRPXRD experiments, the filtered GR samples were carefully dried in the glove box and introduced in 1-mm-diameter Lindeman glass capillaries. They were closed with a glue to avoid any further air oxidation and carried from the LCPME laboratory to ESRF in a gastight container filled with N_2. Samples were mounted on the axis of the diffractometer at the high-resolution powder diffraction beam line ID31 [23] at the ESRF and spun during measurements for increasing powder averaging. HRXRPD patterns were recorded in continuous scanning mode in the 2θ range between 0.25° and 38°. A wavelength of $\lambda = 0.35015(6)$ Å was selected with a double-crystal Si(111) monochromator, calibrated and refined using Si NIST powder ($a = 5.43094$ Å) from the position of the first 10 Si reflections.

The broadening effect on the HRXRPD pattern as a function of the Al^{3+} substitution is illustrated in Fig. 2. An anisotropic line broadening is observed on all the patterns, even for the non-substituted GR(SO_4^{2-}). A microstructural analysis is first performed using the programme FULPROF_suite [24]. The resolution function is estimated by measuring the profile of the Si NIST sample used before for the calibration. The peak shapes are described using the Thomson–Cox–Hasting function (function 7 in Fullprof), allowing a physical interpretation of the line broadening. For that purpose, anisotropic size and strain models included in the programme are used, i.e. a model using the spherical harmonics for the size effect and the generalized strain model. Secondly, the Rietveld analysis is made using a FULPROF_suite programme. Based on the high-resolution data, the four models refined earlier from low-resolution X-ray data [17] are revisited. Model 4 corresponding to the sulphate groups down to the M2 site (1*a*) is retained because it led to the best *R* factors and moreover it is the unique model for which the tetrahedral geometry of the sulphate groups is stable during the refinement. The corresponding Rietveld diagram for the non-substituted compound is reported in Fig. 3. The experimental and refinement parameters for the five analysed compositions are reported in Table 1. For all the refinements, the occupancy factors of the sites 2*c*, 2*e* and 6*k* for the S, O_A (apical) and O_B (basis) atoms, respectively, are fixed with $\frac{1}{2}$ SO_4 in the formula unit in order to be in agreement with the charge balance. Moreover, soft constraints are used for the tetrahedral sulphate groups (d(S–O) = 1.50 Å and O–S–O = 109.5°). Concerning the distribution of Al^{3+} in M1 and M2 sites, preliminary refinements show that the Al^{3+} cations occupy totally the M2 sites where the trivalent iron is supposed to be situated. Thus, final refinement assumes a fixed occupancy factor for Al^{3+} on this site, which is compatible with the formula unit given in Table 1. It must be emphasized that this formula is also compatible with the synthesis conditions and the Mössbauer results (Section 3.2). Finally, for each pattern, 15 dependent intensities parameters are refined. Nevertheless, the number of profile-dependent parameters that are simultaneously refined can vary, depending mainly on the quality of the pattern. For example, for the sample with $y = 0.08$, the number of refined profile parameters is zero, as they are fixed to the value obtained from Pawley's decomposition (profile matching).

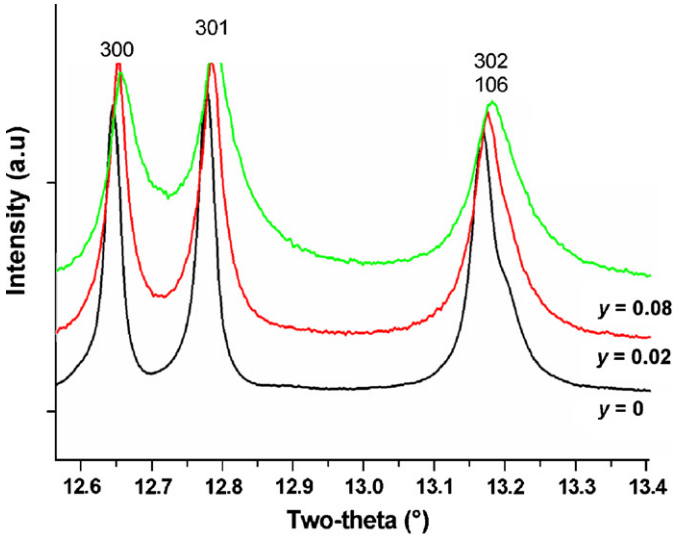

Fig. 2. Illustration of the line broadening for a selected 2θ range of the HRPXRD with the Al^{III} substitution in $(Fe^{II}_2Fe^{III}_{1-3y}Al^{III}_{3y})(OH)_6(SO_4)_{1/2}\cdot 4H_2O$.

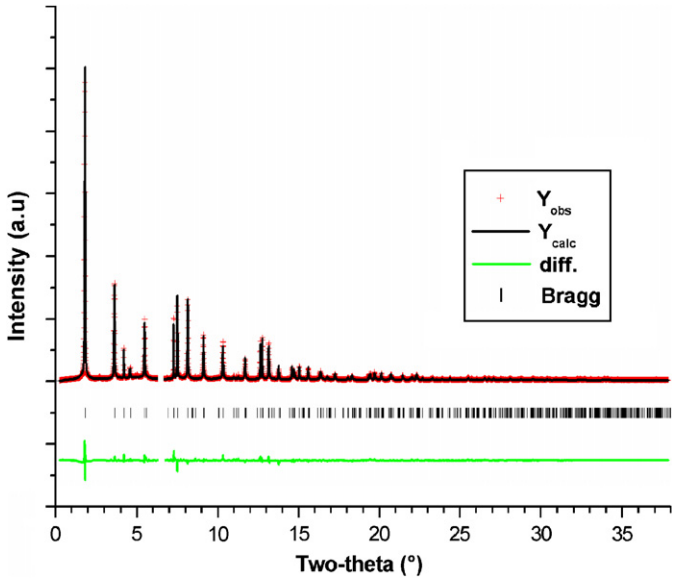

Fig. 3. Rietveld diagram for pure sulphated green rust $Fe^{II}_2Fe^{III}(OH)_6(SO_4)_{1/2}\cdot 4H_2O$.

3. Results

3.1. pH titration curves

The evolution of pH during the co-precipitation of Fe^{II} and Fe^{III} species and the nature of the precipitates were carefully studied in a previous work [22]. The pH curves were characterized by three plateau regions separated by two equivalent points E_1 and E_2. Before point E_1, the Fe^{III} species formed a badly crystallized ferric oxyhydroxide that incorporated small quantity of the sulphate anions [20]. Just after point E_1, the mixed Fe^{II}–Fe^{III} sulphated GR was formed and ferrous hydroxide $Fe(OH)_2$ precipitated before point E_2 when the experiments were carried out at a ferrous molar fraction $x(Fe^{II})_0$ higher than 0.67.

The titration curves of the {Fe^{II}, Fe^{III}, Al^{III}} mixtures exhibit more complicated trends than the aluminium-free {Fe^{II}, Fe^{III}} pH curves: they are characterized by five plateau regions separated by four equivalent points (see in particular curve C of Fig. 4). The first pH plateau is again attributed to the precipitation of Fe^{III} cations, indeed the abscissa of equivalent point E_1 decreases with decreasing quantity of ferric species. The width of a small new plateau situated at pH ~4 increases for an increasing quantity of Al^{III} cations. The first plateau of the pH curve of a reference {Fe^{II}, Al^{III}} mixture (curve D) confirms that the observed new plateau corresponds to the precipitation of the Al^{III} species. Note that the position of equivalent point E_{Al} is identical for all the three experiments; it corresponds to the neutralization of the total amount of trivalent species that is constant. As it will be shown later by Mössbauer spectroscopy, the inflexion of the titration curves around point E_N corresponds to the formation of the Al-GR(SO_4^{2-}) compound. For $x(Al^{III})_0 \leqslant 0.10$, equivalent point E_2 is close to 2 and in good agreement with the formation of an {Al–GR(SO_4^{2-}), $Fe(OH)_2$} mixture. In fact, the experiments were performed at $x(Fe^{II})_0$ higher than 0.67, the excess of Fe^{II} species is expected to form ferrous hydroxide as already observed [22]. For the {Fe^{II}, Al^{III}} mixture (curve D, $x(Al^{III})_0 = 0.33$), abscissa of equivalent point E_2 is shifted at a higher value than 2, meaning that the resulting precipitates cannot be 100% of an Fe^{II}–Al^{III} LDH. As previously discussed [22], such a shift can be attributed to the formation of a spinel structure, i.e. $Fe^{III}_2Fe^{II}O_4$ or $Al^{III}_2Fe^{II}O_4$, which consumes more hydroxyl per mole of cations than the Fe^{II}–Al^{III}

Table 1
Experimental and refinement parameters for of $[Fe^{II}_2(Fe^{III}_{1-3y}Al_{3y})](OH)_6(SO_4)_{1/2}\cdot nH_2O$

y-Value (%)	0	1	2	4	8
F_w (g mol^{-1}) with $n=4$	389.7	388.8	387.9	386.2	382.7
a (Å)	5.50683(3)	5.50462(6)	5.50446(7)	5.50117(5)	5.5021(1)
c (Å)	10.9664(2)	10.9644(3)	10.9658(4)	10.9661(5)	10.9628(5)
V (Å^3)	288.19(1)	287.93(1)	287.95(1)	287.61(1)	287.62(1)
D_x (g cm^{-3})	1.37				
Absorption coefficient ($\mu\times r$)	0.200				
N obs of points	4993	5276	5292	5460	3941
N ind. Ref	463	586	617	584	215
N prof param	14	12	13	13	0[a]
N intensity dep. Param.	15	15	15	15	15
R_p	6.52	8.53	9.46	8.65	9.29
Rw_p	8.85	12.8	12.9	11.6	12.9
R_{bragg}	6.97	7.91	7.60	6.93	9.65
R_F	11.2	10.9	9.50	10.6	14.3
Excluded regions ($2\theta^\circ$)	2.30–3.00	2.40–3.09	2.40–3.09	4.74–5.21	24.0–40.0
	4.77–5.15	4.68–5.17	4.68–5.17	6.18–7.16	
	6.25–6.75	6.20–7.14	6.20–7.14	7.64–7.97	
	32.0–40.0	35.0–40.0	35.0–40.0	35.0–40.0	
Size (anisotropy) (Å)	823 (2397)	443(495)	283(158)	296(214)	263(98)
Strain (anisotropy) $^\circ/^{\circ\circ}$	6.9(2.1)	9.2(6.4)	5.2(3.4)	6.8(3.1)	16.0(2.2)

System $P\bar{3}1m$, $Z=1/2$, $\lambda=0.350018$ Å, 2θ range 0.26–37.87, soft constraints on SO_4^{2-} group.
[a] For the sample with $y=0.08$, the number of refined profile parameters is zero, as they are fixed to the value obtained from the Pawley's decomposition (profile matching).

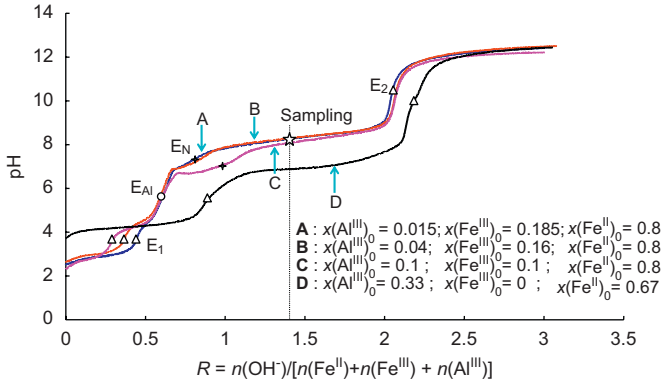

Fig. 4. Evolution of pH during the co-precipitation of {Fe^{II}, Fe^{III}, Al^{III}} mixtures for increasing amount of aluminium, i.e. $x(Al^{III})^0=n(Al^{III})^0/[n(Fe^{II})^0+n(Fe^{III})^0+n(Al^{III})^0]$ where $n(Al^{III})^0$, $n(Fe^{II})^0$ and $n(Fe^{III})^0$ are the mole numbers of the respective soluble cations of the initial solution. For curve D, only Fe^{II} and Al^{III} cations are present in the initial solution.

LDH. The quantity of caustic soda used for the samples analysed by Mössbauer spectroscopy is visualized by a star in Fig. 4: it corresponds to a ratio $R=1.4$ (defined on the figure) that will be shown to be sufficiently low to avoid the formation of both ferrous hydroxide and spinel.

3.2. Mössbauer spectroscopy

The evolution of the Mössbauer spectra as a function of increasing aluminium content is presented in Fig. 5. Contrary to what was previously observed [19], the absence of any magnetic sextet testifies that magnetite Fe_3O_4 does not form in our experimental conditions. The non-substituted compound is characterized by only one ferrous doublet D_1 and one ferric doublet D_3 (Fig. 5a) with the hyperfine parameters given in Table 2. The presence of only two doublets D_1 and D_3 was also correlated with the long-range order of GR(SO_4^{2-}) observed with conventional powder XRD [17]. The formation of ferrous hydroxide $Fe(OH)_2$ can also be ruled out due to the absence, in Fig. 5a, of a second ferrous doublet with a quadrupole splitting value Δ higher than 3 mm s^{-1}. The main feature observed in Fig. 5 is the progressive appearance of a new ferrous doublet D_2 that increases in intensity whereas the area of the ferric doublet D_3 decreases. Therefore, doublet D_2 is attributed to Fe^{II} species that have Al^{III} cations in their close neighbourhoods (see Fig. 6b). As expected, the Al^{III} cations occupy the Fe^{III} sites of the GR structure. By assuming a total occupation of the Fe^{III} sites by the Al^{III} cations present in the initial solution, an expected molar fraction $X(Fe^{III})_{calc}=n(Fe^{III})/[n(Fe^{II})+n(Fe^{III})]$ was calculated that can be directly compared to the relative area of the ferric doublet D_3 in Table 2.

3.3. High-resolution X-ray powder diffraction

3.3.1. Structural models of GR(SO_4^{2-}) and Al-GR(SO_4^{2-})

Structural model of GR(SO_4^{2-}) in which Al^{III} species were allowed to substitute either Fe^{II} or Fe^{III} species was used to perform the Rietveld refinements of the structure of Al-GR(SO_4^{2-}). As expected from the analysis of the Mössbauer results, the model where Al^{III} cations occupy the Fe^{III} sites gives rise to satisfactory results. The refined atomic coordinates and the main distances calculated in the pure and in Al^{III}-substituted GR versus the Al^{III} content are reported in Table 3. A drawing of the structure with the newly determined orientation of the sulphate groups is presented in Fig. 6a. The SO_4^{2-} tetrahedrons are situated between the water molecules with their tops (atoms O_A) at the middle (position 0 0 1/2) of the interlayers. Consequently, their basis is directed toward the iron hydroxide main layers. This orientation implies that the SO_4^{2-} groups are relatively far from iron atoms. The distance between Fe on site M2 (presumably occupied by Fe^{3+} only) and O_B (basis of the SO_4 tetrahedrons) is of 3.288 Å. This distance can be compared to the distance of 3.76 Å between Fe and O-atoms of CO_3^{2-} anions in GR(CO_3^{2-})[18]. However, the Fe–Fe distance in the main layers of both GR is close to 3.18 Å, which is shorter than the Fe–O distance discussed above. Thus, the second neighbours of the octahedrally O-coordinated iron atoms are iron atoms and not the O-atoms of the interlayers anionic species.

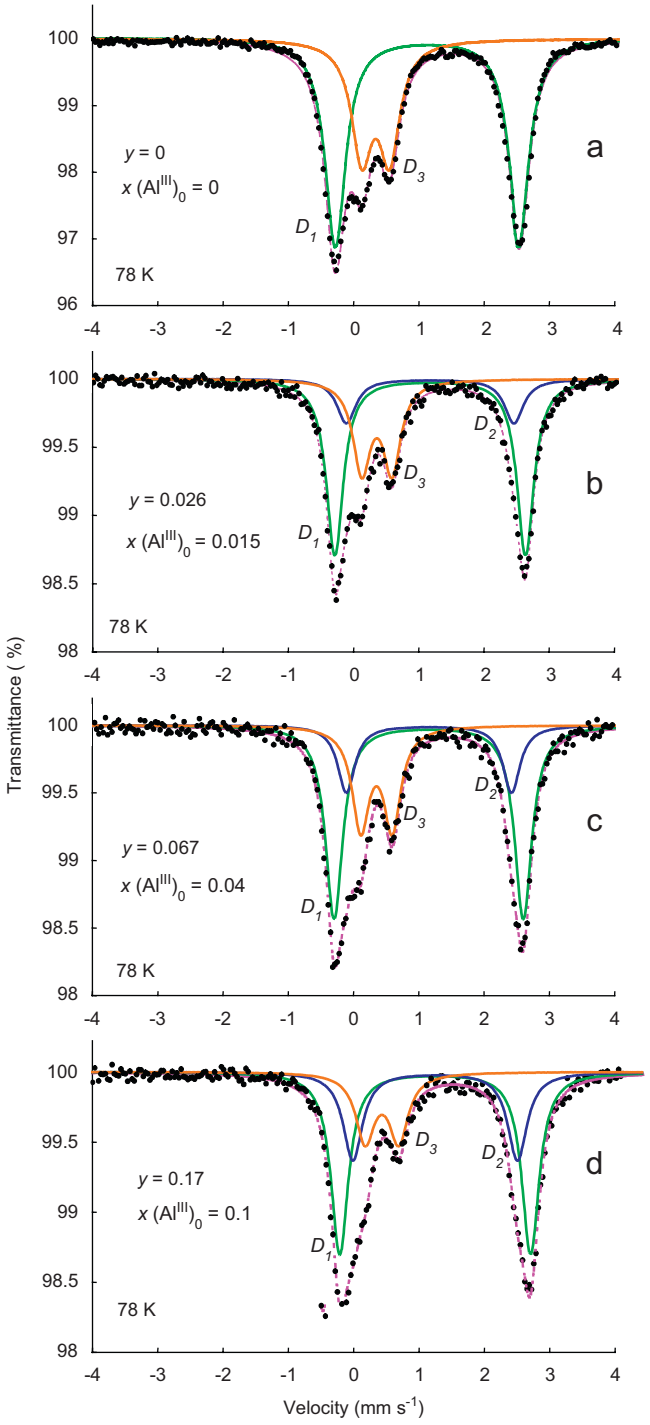

Fig. 5. Evolution of the Mössbauer spectrum for increasing quantity of aluminium inside the hydroxysalt $Fe^{II}_4\ Fe^{III}_{(2-6y)}Al^{III}_{6y}\ (OH)_{12}\ SO_4,\ 8H_2O$.

These second neighbours might have a greater influence on the Mössbauer signals of the iron atoms than the sulphate or carbonate groups in such GRs.

3.3.2. Evolution of the microstructure versus the aluminium content

The microstructural parameters (size and anisotropy, strain and anisotropy) and cell parameters versus Al^{3+} content are reported in Table 1. Despite the fact that Al-GR(SO_4^{2-}) contains a relatively low amount of aluminium, a progressive shift and broadening of all the diffraction lines is observed (Fig. 2). As expected, because ionic radii of Al^{III} cations are slightly smaller than ionic radii of Fe^{III} cations, ($r_{oct}Al^{3+} = 0.535$ Å, $r_{oct}Fe^{3+} = 0.55$ Å), a very small contraction of the unit cell is computed, which corresponds, respectively, to a relative variation of the parameters a and c of 0.09% and 0.03% for the highest aluminium molar fraction $y = 0.08$. A sharp decrease of mean size and anisotropy of the crystals is observed for y values lower than 0.02. The decrease of average apparent crystal size and anisotropy is in good agreement with previous results obtained by TEM [19,20,25]: a crystal size decrease of a factor ~10 for Al-GR(SO_4^{2-}) was observed for a comparable y value of 0.067. It was also shown that non-substituted GR(SO_4^{2-}) exhibits flat hexagonal-shaped crystals and that Al-GR(SO_4^{2-}) was constituted of more rounded crystals in good agreement with the decrease of anisotropy observed here.

3.3.3. Evolution of the structure versus the aluminium content

The water content is 3.80 molecules per unit cell and it remains almost constant as a function of y (Table 3). This refined value confirmed the result found before by low-resolution XRD and by thermal analysis [17]. Nevertheless, the water content for $y = 0.08$ is only 2.4. It is difficult to interpret this difference because the corresponding pattern is much broadened and leads to less accurate results. It must be noted that the strain is relatively constant up to $y = 0.04$ ($\bar{e}$~7‰); it is significantly greater only for $y = 0.08$ ($\bar{e}$~16‰).

The most interesting effect of the Al^{III} substitution is the significant decrease of the M2–OH distances from 2.00 to 1.97 Å when y varies from 0 to 0.04. The distances M1–OH remain greater than that of the former and about constant (d(M1–O-H)≈2.05 Å). This result could be an indication that the M1 and M2 sites are, respectively, occupied by Fe^{2+} and Fe^{3+} cations. It is evident that the XRD cannot separate Fe^{2+} and Fe^{3+} because the contrast X-ray scattering is too low. But, based on the crystallochemistry (ionic charges, interatomic distances) and the Mössbauer results, it appears that both GR(SO_4^{2-}) and Al-GR(SO_4^{2-}) present a cationic order on the two crystallographic sites M1 and M2.

4. Discussion

The formation of Al-GR(SO_4^{2-}) samples was followed by recording the pH during a progressive titration. This kind of approach was used previously for other LDHs by Boclair et al. [26,27]. In most cases the formation of non-substituted M^{II}–M^{III} LDHs follows two separated steps: (i) formation of an initial M^{III} (oxy)hydroxide in acidic condition and (ii) precipitation of the LDHs along a second pH plateau, the value of which is a function of the nature of the M^{II}–M^{III} couple. These results showed that the formation of LDHs does not correspond to a real "co-precipitation" because of the existence of these separated steps. Boclair et al. [27] pointed out that the formation of the M^{II}–Cr^{III} LDHs does not follow this general rule and both divalent and trivalent cations were observed to precipitate together. A separated steps process is also observed for both GR(SO_4^{2-}) and Al-GR(SO_4^{2-}). The addition of aluminium induces the appearance of a new pH plateau corresponding to the precipitation of an aluminium oxy(hydroxide) that occurs after the initial precipitation of the ferric oxyhydroxide. Note that the separated steps formation of the trivalent oxyhydroxides does not prevent the precipitation of Al-GR(SO_4^{2-}) in which all the three cations, i.e. Fe^{II}, Fe^{III} and Al^{III}, are mixed into a unique compound.

When the aluminium content of Al-GR(SO_4^{2-}) is increased, the changes observed by Mössbauer spectroscopy are typical of a cationic substitution. When a divalent cation such as Mg^{II} occupied the Fe^{II} sites of GR(CO_3^{2-}), the appearance of a new

Table 2
Hyperfine parameters of the Mössbauer spectra presented in Fig. 3; δ isomer shift with respect to α-Fe at 298 K; Δ quadrupole splitting; RA relative abundance of each doublet; $X(Fe^{III})_{calc}$ molar fraction of Fe^{III} species calculated relatively to the total amount of iron by assuming a full substitution of the Fe^{III} sites by Al^{III} cations; here $X(Fe^{III})_{calc} = n(Fe^{III})/[n(Fe^{II})+n(Fe^{III})]$

Aluminium content of the initial solution	Expected chemical formula and value of y in the formula $Fe^{II}_4Fe^{III}_{(2-6y)}Al^{III}_{6y}(OH)_{12}SO_4$		δ (mm s^{-1})	Δ (mm s^{-1})	RA (%)	$X(FeIII)_{calc}$ (%)
$x(Al^{III})_0 = 0$	$Fe^{II}_4Fe^{III}_2(OH)_{12}SO_4$	D_1	1.27	2.8	65	
	$Y = 0$	D_3	0.44	0.42	35	33.3
$x(Al^{III})_0 = 0.015$	$Fe^{II}_4Fe^{III}_{1.85}Al^{III}_{0.15}(OH)_{12}SO_4$	D_1	1.28	2.89	56	
	$y = 0.026$	D_2	1.27	2.53	13	
		D_3	0.46	0.45	31	31.6
$x(Al^{III})_0 = 0.04$	$Fe^{II}_4Fe^{III}_{1.6}Al^{III}_{0.4}(OH)_{12}SO_4$	D_1	1.27	2.88	53	
	$y = 0.067$	D_2	1.27	2.52	19	
		D_3	0.47	0.48	28	28.6
$x(Al^{III})_0 = 0.1$	$Fe^{II}_4Fe^{III}_1Al^{III}_1(OH)_{12}SO_4$	D_1	1.27	2.84	56	
	$y = 0.17$	D_2	1.27	2.44	24	
		D_3	0.47	0.49	20	20

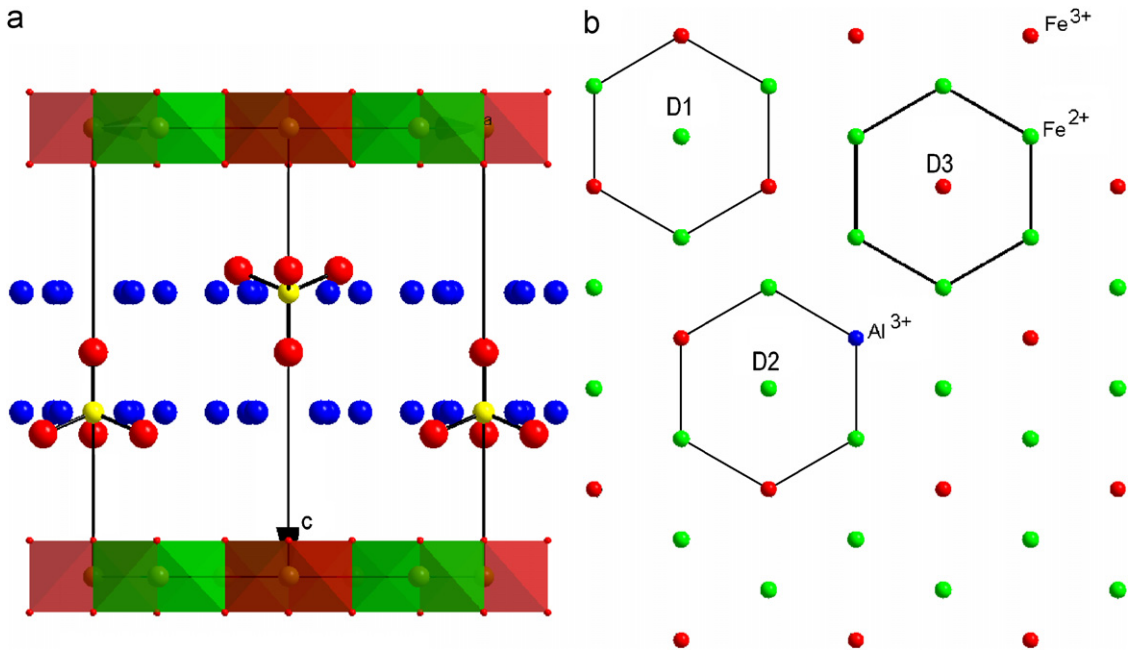

Fig. 6. (a) Projection along [110] of the GR(SO_4^{2-}) structure from synchrotron data. The SO_4^{2-} tetrahedrons are oriented down to Fe^{III} and ordered on the drawing with one SO_4 for two Fe^{III}. The red and green octahedrons are centred by Fe^{III} and Fe^{II} cations, respectively. (b) Hexagonal cations network showing the local metallic environment for Fe^{2+} and Fe^{3+} in the Al^{3+}-substituted GR(SO_4^{2-}) and the corresponding Mössbauer doublets (see text).

ferric paramagnetic doublet was observed [13]. Here the reverse situation exists, while Al^{III} species occupy the Fe^{III} sites, a new ferrous doublet D_2 appears (Fig. 5). This new doublet is due to a change in the second neighbour environment, now Al^{III} atoms in place of Fe^{III} atoms are situated at a distance of ~3.18 Å (Fig. 6b). Of course, Mössbauer spectroscopy detects only local changes around the iron nucleus and an indirect proof of the cationic substitution is given here. Nevertheless, the two last columns of Table 2 show that a good estimation of the cationic substitution level can be obtained from the adjustment of the Mössbauer spectra. It is therefore suitable for analysing cationic substitution in other LDHs containing either iron as a basic cations, e.g. pyroaurite $Mg_6Fe_2(OH)_{16}CO_3 \cdot 4H_2O$, or when Fe species are substituting atoms. Note also that the presence of two ferrous doublets D_1 and D_2 was also reported for non-substituted GR(CO_3^{2-}) [18]. The hyperfine parameters of doublet D_2 ($\delta = 1.27$ mm s^{-1} and $\Delta = 2.63$ mm s^{-1}) reported in this previous study are relatively close to the values corresponding to the doublet D_2 of Al-GR(SO_4^{2-}) (Table 2). On the contrary to GR(SO_4^{2-}), cationic order was not observed for GR(CO_3^{2-}) with HRPXRD [18]. Therefore, effects of the Fe second neighbour distribution in the hexagonal network (Fig. 6b) could also be considered for explaining the origin of doublet D_2 observed for GR(CO_3^{2-}).

The small decrease of cell parameters (Table 1) constitutes a proof that the aluminium cations are really inserted into the brucite-type sheets of the GR structure. The decrease in apparent crystal size with increasing aluminium content confirms the general trends observed in other iron oxyhydroxides such as goethite or lepidocrocite [28]. The microstructural refinement shows clearly that a very small critical amount of aluminium, i.e. $y = 0.02$, is sufficient to lower significantly the crystal size and anisotropy. Interestingly, adding more aluminium does not seem to lead to a further crystal size decrease. Here it is worthwhile to compare the solubility of the various cations: (i) it is well known

Table 3
Refined atomic coordinates and characteristic distances for $Fe^{III}_2(Fe^{III}_{1-3y}Al^{III}_{3\,y})\,(OH)_6(SO_4)_{1/2}\cdot nH_2O$

Value of y in %	0	1	2	4	8
B_{iso}(M1) (site 2*c*)	1.07(5)	0.66(3)	0.68(3)	0.87(4)	3.01(2)
B_{iso}(M2) (site 1*a*)	1.05(9)	2.9(1)	2.7(1)	1.9(1)	0.6(2)
$x(OH^-)$ (site 6*k*)	0.3269(9)	0.3267(11)	0.3256(12)	0.3191(9)	0.316(2)
$z(OH^-)$	0.0799(5)	0.0770(7)	0.0770(7)	0.0810(6)	0.056(8)
$B_{iso}(OH^-)$	2.5(1)	2.7(2)	3.2(2)	2.4(1)	2.0(2)
$x(H_2O)$ (site 12*l*)	−0.165(3)	−0.155(4)	−0.146(4)	−0.153(3)	−0.15(1)
$y(H_2O)$	0.6323(15)	0.647(2)	0.640(2)	0.631(2)	0.624(7)
$z(H_2O)$	0.6334(7)	0.6392(8)	0.637(8)	0.635(7)	0.638(2)
$n(H_2O)$	3.85(4)	3.81(6)	3.81(6)	3.85(5)	2.4(1)
$B_{iso}(H_2O)$	7.0(5)	7.0(8)	6.2(7)	5.2(5)	6(1)
x(S) (site 2*l*)	0.3663(7)	0.3631(8)	0.3625(8)	0.3626(8)	0.3626(9)
O_A on site 1b					
$x(O_B)$ (site 6*k*)	−0.257(1)	−0.261(1)	−0.260(1)	−0.259(1)	−0.261(1)
$z(O_B)$	0.318(1)	0.317(1)	0.316(1)	0.317(1)	0.316(1)
$B_{iso}(SO_4^{2-})$	0.08(13)	1.7(3)	1.2(3)	0.64(2)	13(1)
d(M1–OH) Å	2.050(3)	2.038(5)	2.039(5)	2.074(4)	1.98(1)
d(M2–OH) Å	2.003(5)	1.987(5)	1.981(7)	1.972(4)	1.85(1)
d(S–O_A, S–O_B) Å	1.47, 1.51	1.50, 1.52	1.51, 1.52	1.51, 1.51	1.51, 1.52
O–S–O angles (°)	110.5	109.5	109.3	109.2	109.6

that the Fe^{II} species are much more soluble than both the Al^{III} and Fe^{III} species, (ii) the Al^{III} (oxy)hydroxides are much easily re-dissolved in slightly basic condition in comparison with Fe^{III} oxyhydroxides that dissolve completely only at very high pH (pH > 12) [29]. Therefore, the co-adsorption of soluble Al^{III} and Fe^{II} species onto the initially precipitated ferric oxyhydroxides may play a key role during the formation of Al-GR(SO_4^{2-}). The lowering of the Al-GR(SO_4^{2-}) crystal growth may be linked to the covering rate of aluminium adsorbed on the ferric precipitates. For future works, controlling carefully the low aluminium content in iron(II–III) LDHs (y around 0.01) could be an interesting way to increase the surface reactivity of this compound. Indeed, such a substitution does not change the quantity of Fe^{II} species that are able to reduce many pollutants, e.g. chromate, nitrate, selenate. Nevertheless, because both the microstructural and chemical properties of the surface are then modified, further studies are needed to determine the effect of aluminium on the reactivity of such LDHs.

Acknowledgment

We would like to thank the ESRF for time allocation at beamline ID31.

References

[1] G.W. Brindley, S. Kikkawa, Am. Miner. 64 (1979) 836–843.
[2] A.S. Bookin, V.A. Drits, Clays Clay Miner. 41 (1993) 551–557.
[3] C. de la Calle, C.H. Pons, J. Roux, V. Rives, Clays Clay Miner. 51 (2003) 121–132.
[4] V.A. Drits, A.S. Bookin, Layered Double Hydroxides, Nova Science Publishers, Huntington, 2001, p. 39.
[5] H.C.B. Hansen, S. Guldberg, M. Erbs, C. Bender Koch, Appl. Clay Sci. 18 (2001) 81–91.
[6] S.C.B. Myneni, T.K. Tokunaga, G.E. Brown Jr, Science 278 (1997) 1106–1109.
[7] S. Loyaux-Lawniczak, P. Refait, J.-J. Ehrhardt, P. Lecomte, J.-M.R. Genin, Environ. Sci. Technol. 34 (2000) 438–443.
[8] G.R. Williams, D. O'Hare, J. Mater. Chem. 16 (2006) 3065–3074.
[9] A. Zegeye, G. Ona-Nguema, C. Carteret, L. Huguet, M. Abdelmoula, F. Jorand, Geomicrobiol. J. 22 (2005) 389–399.
[10] J.J. Bravo-Suarez, E.A. Paez-Mozo, S.T Oyama, Quim. Nova 27 (2004) 601–614.
[11] F. Prinetto, G. Ghiotti, P. Graffin, D. Tichit, Micropor. Mesopor. Mater. 39 (2000) 229–247.
[12] G. Carja, R. Nakamura, H. Niiyama, Appl. Catal. A-Gen. 236 (2002) 91–102.
[13] P. Refait, M. Abdelmoula, F. Trolard, J.-M.R. Genin, J.J. Ehrhardt, G. Bourrie, Am. Mineral. 86 (2001) 731–739.
[14] M. Vucelic, W. Jones, G.D. Moggridge, Clays Clay Miner. 45 (1997) 803–813.
[15] A.V. Radha, P. Vishnu Kamath, C. Shivakumara, Acta Crystallogr. B 63 (2007) 243–250.
[16] M. Bellotto, B. Rebours, O. Clause, J. Lynch, D. Bazin, E. Elkaïm, J. Phys. Chem. 100 (1996) 8527–8534.
[17] L. Simon, M. François, P. Refait, G. Renaudin, M. Lelaurain, J.-M.R. Génin, Solid State Sci. 5 (2003) 327–334.
[18] R. Aissa, M. Francois, C. Ruby, F. Fauth, G. Medjahdi, M. Abdelmoula, J.-M. Genin, J. Phys. Chem. Solids 67 (2006) 1016–1019.
[19] R. Aissa, C. Ruby, A. Gehin, M. Abdelmoula, J.-M.R. Genin, Hyperfine Interact. 156/157 (2004) 445–451.
[20] C. Ruby, R. Aïssa, A. Géhin, J. Cortot, M. Abdelmoula, J.-M. Génin, C. R. Geosci. 338 (2006) 420–432.
[21] G.Y. Chao, R.A. Gault, Can. Mineral. 35 (1997) 1541–1549.
[22] C. Ruby, A. Gehin, M. Abdelmoula, J.-M.R. Genin, J.-P. Jolivet, Solid State Sci. 5 (2003) 1055–1062.
[23] A.N. Fitch, Res. Natl. Inst. Stand. Technol. 109 (2004) 133–142.
[24] J. Rodriguez-Carvajal, M.T. Fernandez-Diaz, J.L. Martinez, J. Phys.: Condens. Matter 3 (1991) 3215–3234.
[25] J.-M.R. Génin, A. Rabha, A. Géhin, M. Abdelmoula, O. Benali, V. Ernstsen, G. Ona-Nguema, C. Upadhyay, C. Ruby, Solid State Sci. 7 (2005) 545–572.
[26] J.W. Boclair, P.S. Braterman, Chem. Mater. 11 (1999) 298–302.
[27] J.W. Boclair, P.S. Braterman, J. Jiang, S. Lou, F. Yarberry, Chem. Mater. 11 (1999) 303–307.
[28] U. Schwertmann, J. Friedl, H. Stanjek, D.G. Schulze, Clays Clay Miner. 48 (2000) 159–172.
[29] M. Pourbaix, in: Atlas des équilibres électrochimiques à 25 °C, Gauthier Villars, Paris, 1963.